



## Ion transport restriction in mechanically strained separator membranes

John Cannarella, Craig B. Arnold\*

Department of Mechanical and Aerospace Engineering, Princeton University, Princeton, NJ 08544, USA

### HIGHLIGHTS

- We model and measure the resistance increase associated with separator deformation.
- We show a Bruggeman relation can model tortuosity changes in deformed separators.
- We measure the  $\alpha$  and  $\gamma$  Bruggeman parameters for monolayer separator membranes.
- We measure *in situ* the impedance changes in a pouch cell under applied compression.

### ARTICLE INFO

**Article history:**

Received 27 June 2012

Received in revised form

10 September 2012

Accepted 9 October 2012

Available online 7 November 2012

**Keywords:**

Lithium-ion battery

Mechanical stress

Separator

Power fade

Capacity fade

Tortuosity

### ABSTRACT

We use AC impedance methods to investigate the effect of mechanical deformation on ion transport in commercial separator membranes and lithium-ion cells as a whole. A Bruggeman type power law relationship is found to provide an accurate correlation between porosity and tortuosity of deformed separators, which allows the impedance of a separator membrane to be predicted as a function of deformation. By using mechanical compression to vary the porosity of the separator membranes during impedance measurements it is possible to determine both the  $\alpha$  and  $\gamma$  parameters from the modified Bruggeman relation for individual separator membranes. From impedance testing of compressed pouch cells it is found that separator deformation accounts for the majority of the transport restrictions arising from compressive stress in a lithium-ion cell. Finally, a charge state dependent increase in the impedance associated with charge transfer is observed with increasing cell compression.

© 2012 Elsevier B.V. All rights reserved.

### 1. Introduction

The lithium-ion battery is the preferred energy storage technology in many applications spanning a wide range of size scales from portable electronics to electric vehicles to potentially grid level storage [1]. In many of these applications the battery cells are subjected to mechanical stresses as a result of manufacturing processes (e.g. stack pressure to maintain intimate contact between components [2]), normal operation (e.g. electrode expansion during charge [3] and SEI growth [4]), and abuse during service (e.g. external loading [5]). These stresses occur at the cell level and are distinctly different from the stresses that arise within individual electrode particles, being exerted on the electrode/separator stack normal to the plane of the electrodes. An understanding of cell-level mechanical stresses becomes even more important when

one considers the push to higher capacity electrode materials which exhibit significant lithiation expansions (e.g. 400% for Si [6]).

While there have been a number of studies on stress evolution and fracture within individual electrodes and electrode particles [7–11], only recently have a limited number of studies considered the mechanical behavior of the lithium-ion cell as a whole [12–14]. Computational studies on lithium-ion cells in the literature that have included mechanical phenomena have generally concluded that mechanical stresses have only a small effect on electrochemical performance [15–17]. However, it has recently been demonstrated through *ex-situ* electrochemical studies of transversely compressed pouch cells that mechanical stresses can result in separator deformation, resulting in a significant degradation of cell performance [12]. Battery cells designed for long service lives and operation at high temperatures provide environments where substantial separator deformation can occur as a result of mechanical creep. The importance of the effects of mechanical and thermal stimuli on separators has indeed been the motivation of recent studies on the mechanical behavior of separators [18,19].

\* Corresponding author. Tel.: +1 609 258 0250; fax: +1 609 258 5877.

E-mail address: [cbarnold@princeton.edu](mailto:cbarnold@princeton.edu) (C.B. Arnold).

Here we investigate *in situ* the effects of compressive deformation on the performance of microporous polymer battery separators as well as whole lithium-ion pouch cells through EIS studies of mechanically stressed samples. It is found that applied mechanical compression results in increased cell impedance, which can result in a reduction in performance, especially in high power applications where even small resistances translate into sizeable voltage drops. This increase in impedance can be attributed to decreased ion transport arising from the deformation of both the separator and electrodes.

## 2. Experimental methods

### 2.1. Materials

The separator cells used to measure separator conductivity as a function of strain are constructed by sandwiching 32 layers of wetted separator between two stainless steel foil electrodes and heat sealing the sandwich in an aluminum laminate pouch. Multiple separator layers are used for two reasons: to increase the sensitivity of the impedance measurements by increasing the overall resistance of the separator stack in the cell and to increase the sensitivity of the strain measurements by increasing the overall thickness of the separator stack. The stainless steel foil electrodes are made by cutting the foil into  $2.3 \times 2.3$  cm squares with 3 mm wide leads extending from each end as shown in Fig. 1. The pouch is large enough to accommodate electrolyte that is ejected from the separator pores during compression without building up hydrostatic pressure. Cell construction is performed under argon atmosphere, but testing is conducted in ambient atmosphere. No impedance increase is observed in the separator cells over a period of 24 h in ambient atmosphere indicating a good seal.

Five separators are used in this paper: Celgard 3501, 2400, 2320, and 2340 obtained directly from the manufacturer and GMB 500 mAh pouch cell separator which is removed from GMB 500 mAh LCO-C pouch cells, obtained from Powerstream Technologies, Inc. and manufactured by Guangzhou Markyn Battery Co., Ltd. Celgard 3501 and 2400 are monolayer polypropylene separators while Celgard 2320 and 2340 are trilayer separators containing a layer of polyethylene between two polypropylene layers. Celgard 3501 contains a surfactant coating which is removed by rinsing in DMC prior to separator use. The GMB separator is a monolayer

polyethylene separator fabricated using a dry process, which was determined from FTIR spectra of the separator and SEM images. The electrolyte used in the separator cell experiments is 1 M LiPF<sub>6</sub> in 1:1 (EC:DMC) by wt. obtained premixed from Novolyte Technologies. The conductivity of the electrolyte is measured to be 12.1 mS cm<sup>-1</sup>.

### 2.2. Electrical & mechanical testing

All mechanical testing is performed using an Instron electro-mechanical universal testing machine. Load is applied using spherically seated compression platens to maintain good alignment and is measured using a 50 kN load cell. Strain is measured using the crosshead extension corrected for machine compliance. In order to obtain absolute values of cell thickness during the compression test, the crosshead extension is set to zero by compressing the platens together and zeroing the compressive extension prior to testing. To obtain consistent results, the separator cells are held at a compressive stress of 0.3 MPa until the impedance reaches a steady value. This ensures intimate contact between all separator cell components and allows thermal equilibrium to be reached prior to testing. All mechanical tests are performed using position control.

Impedance measurements are made with a Solartron 1287 electrochemical interface and a Solartron 1260 impedance analyzer using CorrWare Zplot software. Prior to each test, an EIS spectrum is taken to verify that the cell is in good condition. An AC signal of constant frequency is used to measure the real and imaginary components,  $Z'$  and  $Z''$ , of the AC impedance as a function of time.  $Z'$  as a function of strain is obtained by interpolating the strain–time data collected by the Instron Bluehill software to correspond to the impedance–time data collected by the CorrWare Zplot software.

### 2.3. Porosity measurement

Porosity here is defined as the void volume divided by the nominal volume of the separator. The nominal volume is the separator thickness  $l$  multiplied by the cross sectional area  $A$  and the void volume is the difference between the nominal volume and the actual volume of the polymer material comprising the separator. The polymer material volume can be determined by dividing the mass  $m$  of the separator sample by the density of the polymer material  $\rho_m$ . Thus separator porosity  $\Phi$  is given by

$$\Phi = \frac{lA - \frac{m}{\rho_m}}{lA} \quad (1)$$

When calculating the initial porosity  $\Phi_0$  of the separator, an important parameter in subsequent discussion, the initial separator thickness used in Eq. (1) is the separator thickness as determined by Instron platen separation at the onset of the compression test. The polymer material density used in the porosity calculations is the density corresponding to 40% crystallinity, which is the percent crystallinity determined from latent heat measurements of separators made with differential scanning calorimetry [20].

## 3. Theoretical strain-induced separator resistance changes

### 3.1. Model development

To interpret the experimentally observed impedance changes associated with separator strain, a model assuming compression of a separator made of incompressible material is developed. Note that it is separator strain, not stress, which is directly responsible

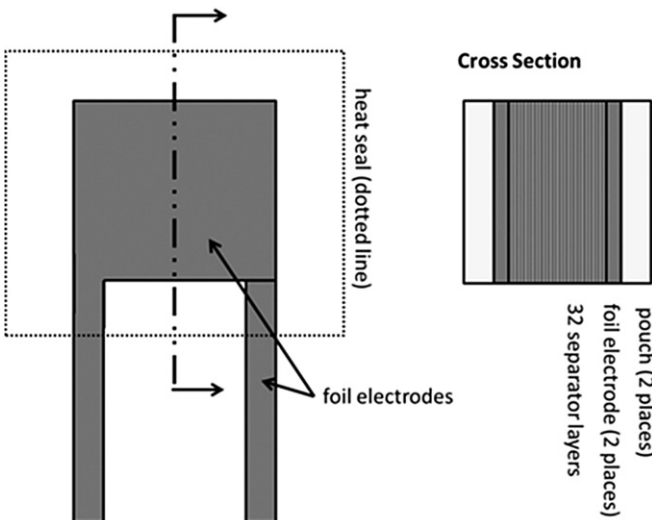


Fig. 1. Schematic of separator cell construction (not to scale).

for pore-closure, because strain describes the deformation of the separator. Applied stress can be used to induce separator strain and can be related to strain through appropriate mechanical models. The resistance of a strained separator, shown schematically in Fig. 2, can be modeled by modifying the basic resistance equation to account for separator porosity and tortuosity as shown in Eq. (2) [21].

$$R = \rho_e \frac{\tau l}{\Phi A} \quad (2)$$

Here  $R$  is the resistance associated with ion transport through the separator,  $\rho_e$  is the resistivity of the electrolyte,  $\tau$  is the separator tortuosity,  $l$  is the separator thickness,  $\Phi$  is the separator porosity, and  $A$  is the area of the electrodes. Tortuosity here is defined as an effective path length arising from mass transport limitations in porous media as described in [22] and can be modeled using a generalized Bruggeman relationship:

$$\tau = \gamma \Phi^{1-\alpha} \quad (3)$$

where  $\gamma$  is a constant and  $\alpha$  is the Bruggeman exponent [23].

The parameters that vary with separator strain are the separator thickness, porosity, and tortuosity, where separator strain is defined as

$$\varepsilon = \frac{l_0 - l_1}{l_0} \quad (4)$$

In this work strain refers to total strain, which includes both elastic (reversible) and plastic (permanent) separator strain. The subscript "1" indicates the parameter in the strained condition and "0" indicates the initial parameter value. Here  $l_0$  is greater than  $l_1$  since compression reduces the separator thickness. From the definition of strain in Eq. (4), the separator thickness as a function of separator strain and initial thickness is simply

$$l_1 = l_0(1 - \varepsilon) \quad (5)$$

An expression for the porosity as a function of strain and initial porosity can be found by assuming the volume of the polymer material comprising the separator membrane remains constant during the application of stress. The constant material volume assumption is valid for the case of the separator membrane because the polymer material comprising the membrane is much more rigid than the membrane itself. Furthermore, the common separator materials polypropylene and polyethylene have relatively high Poisson's ratios of 0.42 [24], which approaches the 0.5 limit for incompressible materials. Finally, polymer creep which would be responsible for the majority of separator deformation over long

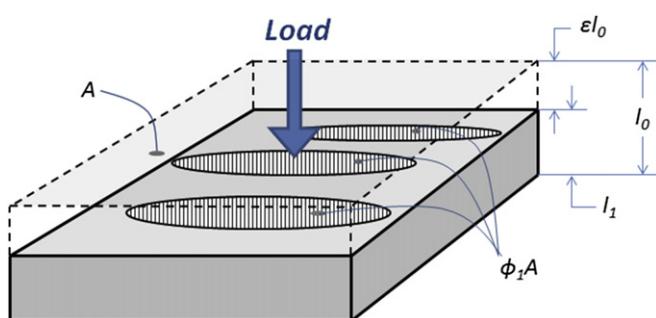


Fig. 2. Schematic of a strained separator under an applied load labeled with nominal area  $A$ , effective void area  $\phi_1 A$ , initial thickness  $l_0$ , strained thickness  $l_1$ , and separator deformation  $\varepsilon l_0$ .

times during battery operation, is a flow process which occurs at constant material volume. Thus we can arrive at an expression for the porosity of a deformed separator by equating the volumes of the polymer material in the separator at the strained and unstrained states:

$$V_1 = A(1 - \Phi_1)l_1 = V_0 = A(1 - \Phi_0)l_0 \quad (6)$$

Substituting Eq. (5) into Eq. (6) and solving for  $\Phi_1$  gives porosity as a function of strain:

$$\Phi_1 = \Phi_0 \left( \frac{1 - \varepsilon/\Phi_0}{1 - \varepsilon} \right) \quad (7)$$

Substituting Eq. (7) into Eq. (3) and factoring out the initial tortuosity gives tortuosity as a function of strain:

$$\tau_1 = \tau_0 \left( \frac{\Phi_1}{\Phi_0} \right)^{1-\alpha} = \tau_0 \left( \frac{1 - \varepsilon/\Phi_0}{1 - \varepsilon} \right)^{1-\alpha} \quad (8)$$

Eqs. (5), (7), and (8) show that there is a competition between decreasing resistance through decreased thickness and increasing resistance through decreased porosity and increased tortuosity in a strained separator. The porosity and tortuosity effects tend to dominate the thickness reduction effect, and consequently resistance increases with separator strain. Note that the decrease in pore volume of the separator requires that electrolyte flow out of the separator pores during compression. The separator resistance change as a function of strain is then given by substituting Eqs. (5), (7), and (8) into Eq. (2) and rearranging:

$$\begin{aligned} \Delta R &= R_1 - R_0 = \rho_e \frac{l_0 \tau_0}{A \Phi_0} \left( \frac{(1 - \varepsilon)^{\alpha+1}}{(1 - \varepsilon/\Phi_0)^\alpha} - 1 \right) \\ &= R_0 \left( \frac{(1 - \varepsilon)^{\alpha+1}}{(1 - \varepsilon/\Phi_0)^\alpha} - 1 \right) \end{aligned} \quad (9)$$

From Eq. (9), one can see that the resistance change is dependent on four parameters:  $\varepsilon$ ,  $\alpha$ , initial separator resistance  $R_0$ , and initial separator porosity  $\Phi_0$ .  $R_0$  can be obtained from impedance measurements,  $\varepsilon$  can be controlled using a compression testing machine, and  $\Phi_0$  can be measured using mass, volume, and density considerations as detailed in Section 2.3. The Bruggeman exponent  $\alpha$  is not known *a priori* and must be determined by curve fitting Eq. (9) to experimental data. By using mechanical strain to experimentally vary the porosity of the separator we can obtain  $\alpha$  independently of  $\gamma$  similar to measurements made by Thorat et al. of  $\alpha$  and  $\gamma$  for electrode films [23].

## 4. Results and discussion

### 4.1. Transport reduction in strained separators

The impedance to ion transport through the separator is determined by measuring the AC impedance of separators immersed in electrolyte contained in a separator cell as described in Section 2.1. The EIS spectrum for a separator cell, shown in Fig. 3, exhibits a curve characteristic of a double layer capacitor. As the separator cell is compressed,  $Z'$  increases uniformly over the frequency range shown in the figure, indicating that one can measure resistance change as a function of time using any signal with a constant frequency in this range. Signals with frequencies between 40 kHz and 100 kHz are chosen to make temporal resistance measurements, which correspond to impedance values having the lowest magnitude of  $Z''$  in the linear portion of the Nyquist plot. Since the  $Z''$  change is much smaller than the  $Z'$

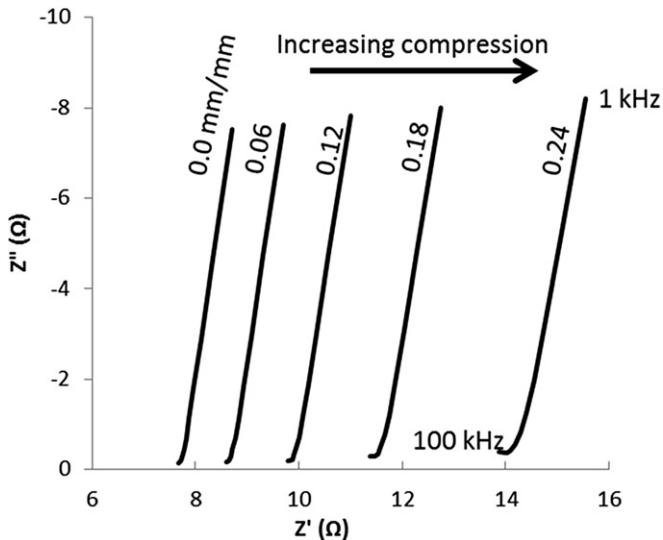


**Fig. 3.** Typical Nyquist plot from 100 kHz to 1 kHz of a separator cell at different levels of strain showing a uniform increase of  $Z'$  with compression over a range of frequencies.

change, we can assume that there are no  $Z'$  changes arising from the fact that the capacitance of the system is changing with strain. While resistance changes can be measured using points in the linear region of the Nyquist plot, measurements of absolute values of resistance (e.g.  $R_0$  measurements) are made by extrapolating the linear region of the plot to the  $Z'$  axis and taking the intercept to be the resistance value.

A typical plot of the resistance increase normalized by initial resistance  $R_0$  of a Celgard 3501 separator cell as a function of total separator strain is shown in Fig. 4. Similar curves are obtained for the other separator samples studied in this work. This plot spans separator porosity ranging from an initial value of 0.51 at 0 strain to a final value of 0.23 at 0.35 strain, which can be calculated from the strain data using Eq. (7). A curve fit of Eq. (9) normalized by  $R_0$  taking  $\alpha$  as a fitting parameter is overlaid on the experimental data and shows good agreement. The  $\Phi_0$  value in the curve fit is fixed to 0.51, which is the experimentally measured value for Celgard 3501 separator. The curve fit is sensitive to  $\Phi_0$  and errant  $\Phi_0$  values result

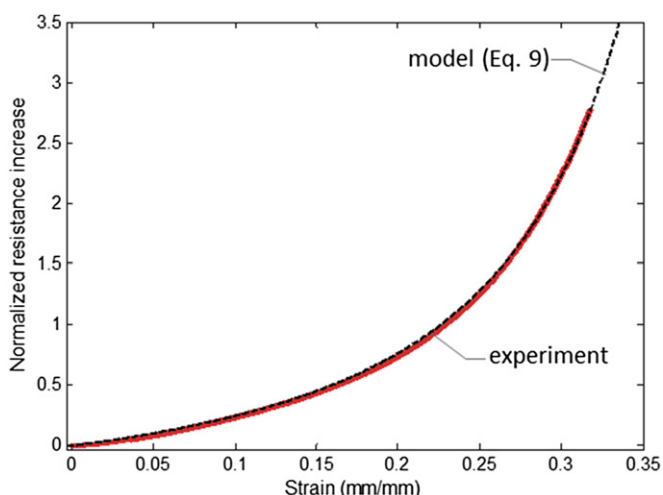


**Fig. 4.** Curve fit of Eq. (9) normalized by  $R_0$  taking  $\alpha$  as a fitting parameter for experimental resistance–strain data of Celgard 3501 separator.

in visually poor fits regardless of  $\alpha$ . Note that the strain–resistance plot shown in Fig. 4 is for a single separator sample; the average values of parameters characterizing the strain–resistance curves for all separator samples tested in this work over many trials are summarized in Table 1 along with their standard deviations.

The agreement between the model and experiment validates the assumptions made in developing the model and indicates that the Bruggeman relationship can be used to predict the tortuosity change of a separator due to pore-closure resulting from deformation. While it is possible to determine the value of the Bruggeman exponent  $\alpha$  for a separator from curve fits of the resistance–strain data according to Eq. (9), the resistance–strain curves do not depend on the  $\gamma$  parameter. To determine  $\gamma$  it is necessary to construct tortuosity–porosity curves for each separator sample to allow for a direct fit of Eq. (3), the modified Bruggeman relation, as has been done in previous tortuosity studies investigating electrode tortuosity [22,23]. Tortuosity–porosity curves for each of the five separator samples studied in this work are shown in Fig. 5. These curves are obtained by using Eq. (2) to calculate tortuosity from resistance data and using Eq. (7) to convert strain data to porosity data. Both calculations used to transform the resistance–strain curves to tortuosity–porosity curves assume the initial porosities shown in Table 1, which is necessary to determine porosity from strain using Eq. (7). Note that the initial porosity values correspond to the porosity of the separators when compressed to 0.5 MPa, the ratcheting stress that is exerted by the Mitituyo micrometers when measuring thickness. The initial porosities used for the trilayer membranes, Celgard 2320 and 2340, are the porosity values provided by the manufacturer literature [25].

The tortuosity–porosity curves for the monolayer separator samples presented in Fig. 5 are overlaid with curve fits of Eq. (3). The success of the fit for the monolayer membranes is expected since Eq. (3) is used in the development of Eq. (9), which successfully describes the resistance–strain data for these membranes. The Bruggeman parameters  $\gamma$  and  $\alpha$  obtained for the monolayer separators from curve fits of the tortuosity–porosity data are tabulated in Table 1. The modified Bruggeman relation is unable to correlate tortuosity to porosity of the trilayer membranes, which is not surprising given that Eq. (3) does not account for the possibility of distinct layers with different properties within a single membrane. Because the curve fit is unsuccessful for the trilayer membranes, Table 1 only reports initial tortuosity values for Celgard 2320 and 2340, and no attempt is made at determining the Bruggeman parameters for these separators.

The Bruggeman parameters determined in this study for the monolayer membranes differ from the parameters reported in previous studies of separator tortuosity. This is because previous studies measure tortuosity only at a single porosity, whereas in this study porosity is varied by straining the separator. When measuring tortuosity at a single porosity, the Bruggeman parameters cannot be determined independently, and thus  $\gamma$  is typically assigned a value of unity [23]. Nevertheless, the tortuosity value itself should not be affected by the arbitrary assignment of  $\gamma$ , and the initial (0.5 MPa) tortuosity values shown in Table 1 are in agreement with previous reports [23]. As is typical with studies on transport in battery materials, the Bruggeman exponents differ from the commonly assumed value of 1.5.

#### 4.2. Transport reduction in strained pouch cells

A rise in impedance with increasing compression can also be observed for lithium-ion pouch cells through AC impedance testing. A typical Nyquist plot (not shown here) for the GMB 500 mAh LCO-C pouch cells used in this work exhibits the usual features characteristic of a lithium-ion cell: a high frequency intercept

**Table 1**

Experimentally measured separator parameters. All initial parameters are measured under a uniaxial compression of 0.5 MPa.

Sample	$l_0$ ( $\mu\text{m}$ )		$\phi_0$		$\tau_0$		$\alpha$		$\gamma$	
	Avg	Stdev	Avg	Stdev	Avg	Stdev	Avg	Stdev	Avg	Stdev
Celgard 2400	25.9	0.23	0.372	0.0090	2.73	0.19	2.43	0.10	0.667	0.082
Celgard 3501	24.8	0.19	0.515	0.0036	2.72	0.11	3.33	0.13	0.580	0.053
GMB 500 mAh	20.9	0.28	0.423	0.0061	3.39	0.060	1.77	0.080	1.77	0.093
Celgard 2320	20.6	0.10	0.41 <sup>a</sup>	—	4.51	0.022	—	—	—	—
Celgard 2340	39.7	0.23	0.45 <sup>a</sup>	—	3.88	0.073	—	—	—	—

<sup>a</sup> Obtained from manufacturer literature [25] in lieu of measurement.

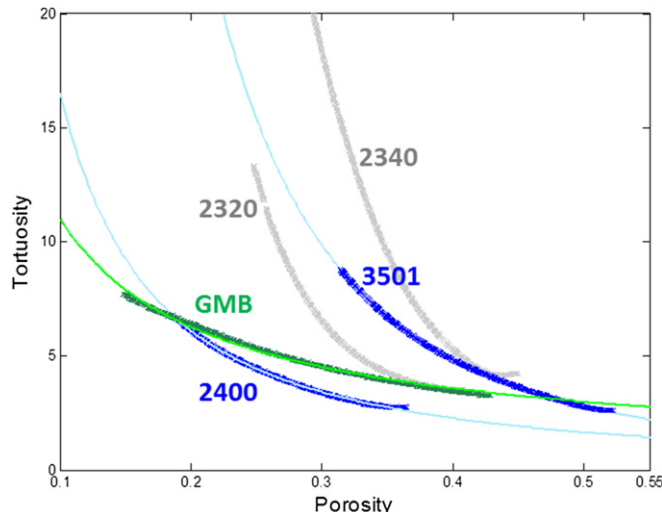


Fig. 5. Tortuosity–porosity plots for different separators (GMB pouch cell separator and Celgard 2400, 3501, 2320, and 2340 separators).

corresponding to electronic and ionic resistances, a mid-frequency arc corresponding to double layer capacitance in parallel with charge transfer, and a low frequency spike associated with the Warburg impedance [26]. To characterize the effects of mechanical compression on the electrochemical performance of the pouch cells, the cells are loaded to a given stress and held at that stress level while an impedance spectrum is taken. Impedance spectra at three different stress levels are shown in Fig. 6, with the real and imaginary components plotted separately as a function of decreasing frequency. A descending frequency axis is chosen so that the frequency domain spectra resemble the familiar Nyquist plot impedance spectrum shape.

From Fig. 6a one sees that the real component of the impedance  $Z'$  increases with stress across all frequencies. The  $Z'$  increase is larger at lower frequencies than at high frequencies. By comparison with an equivalent circuit model for a lithium-ion cell, the increase at high frequencies corresponds to an increase of resistance due to reductions in ion transport in the electrolyte phase and this impedance is present over all frequencies [26]. The additional increase at lower frequencies is attributed to an increase in charge transfer resistance [26]. There is a slight increase in the imaginary component of impedance with stress in Fig. 6b, which indicates a small decrease in double layer capacitance. More importantly, Fig. 6b shows that the frequencies at which the imaginary component of the impedance goes to zero, corresponding to the  $Z'$  axis intersections of the EIS spectrum in the Nyquist plot, remain constant with stress. This indicates that an AC signal set to the frequency corresponding to the Nyquist plot  $Z'$  axis intercepts can be used to continuously monitor the electrolyte and charge transfer resistances in time as mechanical strain is applied and removed from the pouch cell. If a constant strain-rate loading protocol is used, then it is possible to obtain curves of impedance as a function of strain. For the case of the GMB 500 mAh pouch cell, the frequency corresponding to the electrolyte resistance is 5 kHz and the frequency corresponding to the charge transfer resistances is 2 Hz which can be seen in Fig. 6.

Plots of the electrolyte and charge transfer resistances as a function of battery deformation are shown in Fig. 7. In this figure the pouch cell is compressed from an initial stress level of 0.5 MPa to a final stress level of 15 MPa using a constant strain-rate loading protocol. It is observed that the strain-induced impedance increase at high frequencies is independent of battery state of charge. The independence from state of charge is expected since high frequency impedance is dominated by the separator and electrolyte, components whose properties do not vary with charge state. However, the strain-induced increase in charge transfer resistance is dependent on state of charge, with lower states of charge showing higher

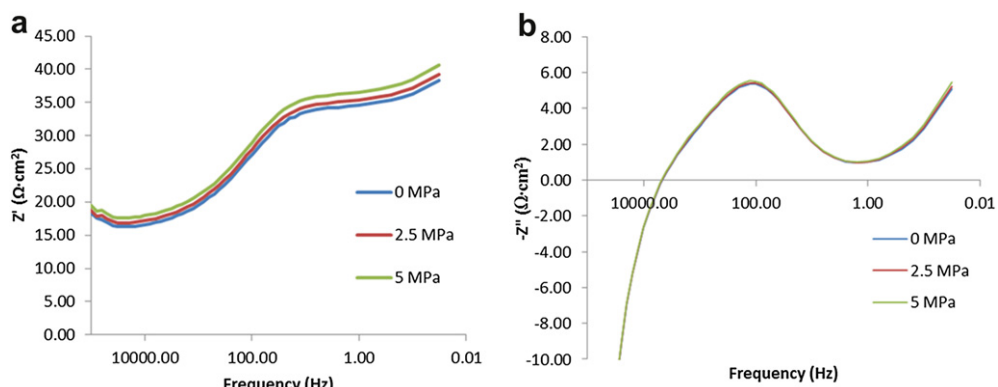


Fig. 6. Impedance spectra for a GMB 500 mAh battery from 5 kHz to 10 mHz with (a) the real component  $Z'$  and (b) the imaginary component  $-Z''$  plotted in the frequency domain at different stress levels.

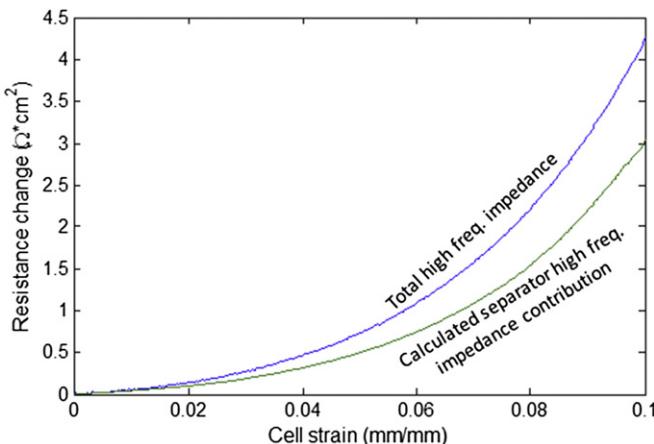


Fig. 7. Plot of the high frequency (5 kHz) impedance of a GMB 500 mAh pouch cell as a function of cell strain with the calculated impedance contribution due to separator compression overlaid.

impedance increases as can be seen in Fig. 8. Note that here charge transfer resistance is defined as the 2 Hz impedance minus the 5 kHz impedance so that the resistance curve in Fig. 8 does not contain contributions from separator compression. Similar reductions in the kinetics of stressed lithium-ion intercalation electrodes have been observed in studies investigating the use of such electrodes as actuators [27].

To better understand the resistance increase at high frequencies, the expected resistance increase due to an increase in separator resistance with compression is plotted in Fig. 7 alongside the experimentally measured high frequency resistance for the pouch cell. The expected separator resistance increase is calculated using Eq. (9) using the experimentally measured initial porosity and Bruggeman exponent for the GMB separators. The initial resistance  $R_0$  used in determining the expected resistance increase due to the separator in the pouch cell is calculated using the experimentally measured resistivity ( $150 \Omega \cdot \text{cm}$ ) of the electrolyte used in the GMB cells and the measured separator geometry inside the cell. Since the separator strain during the pouch cell compression test cannot be directly measured, the separator strain is calculated by comparing the stress measured during the compression test of the GMB pouch cell to a stress–strain curve of the separator obtained from an

independent mechanical compression test of a GMB battery separator wetted in electrolyte. This procedure is valid for the uniaxial loading conditions in this study because all battery components are in series with each other and therefore experience the same stress as is applied to the pouch cell. Comparison of the two curves in Fig. 7 shows that separator deformation accounts for the majority of the high frequency impedance increase during compression of a pouch cell. The remaining proportion of the high frequency impedance increase is likely due to compression of the electrodes, possibly from a reduction in electrolyte–phase transport in within the deformed electrode pore network.

## 5. Conclusions

Here the effects of compressive deformation on the ionic transport characteristics of lithium-ion cells are shown through impedance studies of separator cells and pouch cells undergoing mechanical compression. It is observed through EIS studies that pouch cell impedance increases with compression due to decreases in ion transport through the deformed pore networks of the separator, and to a lesser extent the electrodes. A SOC-dependent increase in the cell's charge transfer resistance with increasing compression is also observed. The impedance increases associated with the separator can be predicted by accounting for porosity and thickness changes of the separator in the resistance equation and assuming all deformation occurs with constant material volume. The constant material volume assumption is justified by considering the separator deformation mechanisms during compression and realizing that the separator network is much more compliant than its constituent polymer material. The Bruggeman relation is shown to provide a good description of the tortuosity of a separator undergoing compressive deformation and the Bruggeman parameters for various separators under compression are measured experimentally. Knowledge of these parameters will aid in modeling transport in lithium-ion cells held under cell-level mechanical stress.

The implication of the pore-closure induced resistance increases is that lithium-ion cells that are held under compressive mechanical stress, whether due to external stresses such as applied loads or internal stresses such as electrode expansion and SEI growth, can have higher impedances if significant pore-closure occurs. Furthermore, localized pore-closure of the separator can result in inhomogeneous current distribution which can result in non-uniform electrode utilization. If the stress is held for long periods of time, creep processes can contribute to pore-closure in addition to elastic compression [12]. Such processes would be further aggravated by high temperatures that can arise from battery operation or environmental heat sources. The gradual closure of pores over the life time of a battery undergoing mechanical compression ultimately will result in a decrease in rate capability, especially in high power applications.

## Acknowledgments

J.C. acknowledges the Department of Defense (DoD) for support through the National Defense Science & Engineering Graduate Fellowship (NDSEG) Program. We acknowledge the Princeton University Siebel Energy Grand Challenge and the Carbon Mitigation Initiative for financial support.

## References

- [1] B. Dunn, H. Karmath, J.-M. Tarascon, *Science* 18 (2011) 928–935.
- [2] W. van Shalkwijk, B. Scrosati, *Advances in Lithium-Ion Batteries*, first ed., Kluwer Academic Publishers, New York, 2002.

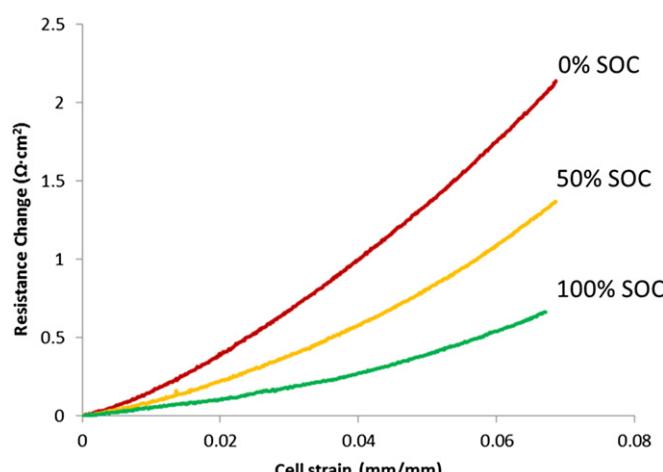


Fig. 8. Plots of the charge transfer resistance as a function of cell strain for a GMB 500 mAh pouch cell at different charge states. The charge transfer resistance is defined here as the 2 Hz impedance minus the 5 kHz impedance (Fig. 7).

- [3] Y. Koyama, T.E. Chin, U. Rhyner, R.K. Holman, S.R. Hall, Y.-M. Chiang, *Adv. Funct. Mater.* 16 (2006) 492–498.
- [4] J. Vetter, P. Novak, M.R. Wagner, C. Veit, K.-C. Moller, J.O. Besenhard, M. Winter, M. Wolfhart-Mehrens, C. Volger, A. Hammouche, *J. Power Sources* 147 (2005) 269–281.
- [5] T. Pereira, Z. Guo, S. Nieh, J. Arias, H. Thomas Hahn, *Comp. Sci. Technol.* 68 (2008) 1935–1941.
- [6] B.A. Boukamp, G.C. Lesh, R.A. Huggins, *J. Power Sources* 128 (1981) 725–729.
- [7] Y.-T. Cheng, M.W. Verbrugge, *J. Power Sources* 190 (2009) 453–460.
- [8] X. Zhang, W. Shyy, A. Marie Sastry, *J. Electrochem. Soc.* 154 (2007) A910–A916.
- [9] J. Christensen, J. Newman, *J. Solid State Electrochem.* 10 (2006) 293–319.
- [10] V.A. Sethuraman, M.J. Chon, M. Shimshak, V. Srinivasan, P.R. Guduru, *J. Power Sources* 195 (2010) 5062–5066.
- [11] S.W. Lee, M.T. McDowell, L.A. Berla, W.D. Nix, Y. Cui, *Proc. Natl. Acad. Sci. U.S.A.* 109 (2012) 4080–4085.
- [12] C. Peabody, C.B. Arnold, *J. Power Sources* 196 (2011) 8147–8153.
- [13] D. Shi, X. Xiao, X. Huang, H. Kia, *J. Power Sources* 196 (2011) 8129–8139.
- [14] X. Xiao, W. Wu, X. Huang, *J. Power Sources* 195 (2010) 7649–7660.
- [15] J. Christensen, *J. Electrochem. Soc.* 157 (2010) A366–A380.
- [16] S. Golmon, K. Maute, M.L. Dunn, *Comput. Struct.* 87 (2009) 1567–1579.
- [17] A. Awarke, S. Lauer, M. Wittler, S. Pischinger, *Comput. Mater. Sci.* 50 (2011) 871–879.
- [18] A. Sheidaei, X. Xiao, X. Huang, J. Hitt, *J. Power Sources* 196 (2011) 8728–8734.
- [19] C.T. Love, *J. Power Sources* 196 (2011) 2905–2912.
- [20] C. A. Peabody, PhD thesis, Princeton University, USA, 2011.
- [21] P. Arora, Z. Zhang, *Chem. Rev.* 104 (2004) 4419–4462.
- [22] D. Kehrwald, P.R. Shearing, N.P. Brandon, P.K. Sinha, S.J. Harris, *J. Electrochem. Soc.* 158 (2011) A1393–A1399.
- [23] I.V. Thorat, D.E. Stephenson, N.A. Zacharias, K. Zaghib, J.N. Harb, D.R. Wheeler, *J. Power Sources* 188 (2009) 592–600.
- [24] J.E. Mark, *Polymer Data Handbook*, second ed., Oxford University Press, Inc., New York, 2009.
- [25] [www.celgard.com](http://www.celgard.com), June 2012.
- [26] E. Barsoukov, J. Macdonald, *Impedance Spectroscopy: Theory, Experiment and Applications*, second ed., Wiley Interscience, New York, 2005.
- [27] T.E. Chin, U. Rhyner, Y. Koyama, S.R. Hall, Y.-M. Chiang, *Electrochem. Solid State Lett.* 9 (2006) A134–A138.